High-pressure evolution of novel R_2CuTiO_6 (R = Tb – Lu) perovskite phases

Linda Sederholm [a], Edmondo Gilioli [b], Davide Delmonte [b], Ayako Yamamoto [c], Maarit Karppinen [a,*]

[a] Department of Chemistry and Materials Science, Aalto University, FI-00076, Espoo, Finland
[b] Institute of Materials for Electronics and Magnetism, CNR, Parma, A 43124, Italy
[c] Graduate School of Engineering and Science, Shibaura Institute of Technology, Saitama, 337-8570, Japan

ABSTRACT

Perovskite oxides of the R_2CuTiO_6 type with a trivalent rare earth element (R) at the A-cation site and co-occupancy of the B-cation site with the Jahn-Teller d^9 Cu^{2+} and d^0 Ti^{4+} transition metals, provides an interesting playground for various chemical and physical phenomena. However, conventional solid-state synthesis under ambient-pressure (AP) yields the perovskite structure only for the largest R constituents from La to Gd; with the smaller rare earth elements (Y, Tb–Lu) a non-perovskite (hexagonal $BaTiO_3$-type) structure is formed. Here we demonstrate that through high-pressure (HP) high-temperature treatment, the hexagonal AP structure can be converted into a distorted (orthorhombic) perovskite structure for all the smaller R constituents. The critical pressure needed for the conversion increases with decreasing R^{3+} ion size, up to ca. 6 GPa for R = Lu. Moreover, a novel intermediate phase is found to form for most of the R constituents when pressures lower than the critical pressure are applied. We have employed both X-ray diffraction and UV–vis spectroscopy analyses to systematically follow the phase formation schemes for the different R constituents.

1. Introduction

The perovskite structure is one of the fundamental crystal structures for inorganic multi-metal oxides. In its simplest, ideal form, the perovskite formula ABO_3 denotes a cubic lattice of corner-sharing BO_6-octahedra of oxygen-bonded B-site metal cations, with the 12-coordinated central space occupied by a larger A-site metal cation. The structure is highly tolerant of chemical modifications on each of the crystallographic sites, readily accepting various co-occupancy schemes [1]. At the fixed-ratio occupancies of 1:1, 1:2 and 1:3 on one of the cationic sites, numerous exciting families of double, triple and quadruple perovskites with an intriguing property palette have been synthesized [2–4]. Especially for the so-called B-site double perovskites of the $A_2B'B''O_6$ formulae [5], several cationic ordering patterns are possible, and accordingly exciting properties such as ferrimagnetism and spin-glass like properties in Pb_2NiReO_6 [6] and $(Ca,Sr)_2CoOsO_6$ [7], and angle-dependant super-exchange in $(Ba,Sr)_2Cu(W,Te)O_6$ [8] have been realized.

For double perovskites exhibiting various degrees of cationic order [9–12], an ordering parameter has been introduced to describe the adherence to a given atomic ordering pattern, most commonly rock-salt, layered, or columnar order. Cationic order appears as a result of sufficient incentive from thermodynamical parameters, bond strain, and coulombic repulsion. In addition, special cases of electronic effects may incentivise certain patterns, such as Jahn-Teller distortion sometimes promoting layered or columnar ordering [9].

The range of possible elemental combinations that can crystallize into a perovskite structure is limited by geometrical factors that derive from elemental radii. Best known is the Goldschmidt tolerance factor [13], that uses Shannon ionic radii [14] to evaluate whether a perovskite might form by a formula derived from the geometrical structure of an ideal perovskite:

$$t = \frac{r_A + r_O}{\sqrt{2}(r_B + r_O)}$$

Here, r_A, r_B, and r_O are the ionic radii of the A and B cations and oxygen anion, respectively; for a co-occupied site the weighted mean radius of the occupants is used. An ideal perovskite has $t = 1$ and a perfectly cubic symmetry, while $t > 1$ indicates an oversized A-site occupant which will generally tear apart the B–O-bonding network. Moderately undersized A-site occupants leading to $t < 1$ can be accommodated with various structural distortions, whereby the network of BO_6-octahedra often takes on various tilting patterns as described by Glazer's notation [15]. Thus, the lower limit of the tolerance parameter is derived from geometrical limits set by the octahedral network and can be described via the octahedral factor $\mu = r_B/r_o$. Filip et al. [16] have given a detailed description of the various formability limits derived from factors concerning the BO_6-octahedron network. The combined

---

* Corresponding author.
 E-mail address: maarit.karppinen@aalto.fi (M. Karppinen).

limitations result in an allowed range of phase formability for the perovskite phase, which we take to include also distorted versions of the ideal perovskite structure as long as the atomic interconnectivity remains intact.

Outside of the perovskite formability range, the most common structures taken on by the ABO$_3$ stoichiometries are various structures with hexagonal symmetry, where the A- and B-coordination polyhedra follow various stacking and connectivity patterns. Some of these stacking patterns express local similarities to the perovskite structure, for example the series of structures presented by Syono et al. [17] and by Vente & Battle [18] where the BO_6-octahedra within the unit cell are grouped into corner-sharing and edge- or face-sharing structural regions. Meanwhile, in the structure first described as "hexagonal BaTiO$_3$" [19] and later refined by Yakel et al. [20] for a series of $RMnO_3$ compounds, the cations possess reduced coordination numbers of CN(A)=7 and CN(B)=5, and the layers of corner-sharing BO_5 trigonal bipyramids are not connected. This same hexagonal structure with space group $P6_3cm$ has since been reported for a long list of compounds [17,21–30]; in this article, we refer to this structure as "hexagonal" structure or phase.

High pressure can influence the practical formability of perovskites, as the perovskite structure is among the densest atomic packings available for metal oxides [17,23,29–33]. Thus, an originally "unsuitable" combination of t, μ, and $\Delta\mu$ can be stabilized under (ultra)high-pressure conditions, by compressing the material to a state where the dense perovskite phase is promoted (and its formation can be aided by high temperature). If the internal strain is not too high for the interatomic bonds in the structure, the phase will survive pressure release in metastable condition [34,35]. In double perovskites, the high-pressure treatment can also influence the cationic ordering both negatively and positively, depending on how the ordering-determining factors are influenced by compression of the atomic distances [36].

Many studies into the high-pressure stabilization of the perovskite structure have focused on sample series with a rare-earth element (R) at the A-site. For example, series of $RMnO_3$ [23,37,38] and $RInO_3$ [34,35, 39] perovskites have been formed using pressures up to 20 GPa; all of these are reported to form in the hexagonal phase at ambient pressure. An investigation of the reported high-pressure phase conversion studies performed on the MTO_3 system (M = s-, d-, or f-block element, T = transition metal) implies that the absolute limit of formability for perovskites, even when physically compressed, would be around $t \approx 0.8$ [17,23,34,35,37–45].

Recently, we reported a successful high-pressure (4 GPa) conversion of hexagonal Y$_2$CuTiO$_6$ to an orthorhombic perovskite structure similar to the structure seen in the R_2CuTiO_6 system for the largest R constituents (La–Gd) after ambient-pressure synthesis [46]. The R_2CuTiO_6 system has been considered as an interesting model system for electronic/magnetic studies owing to its Jahn-Teller d^9 Cu^{2+}/d^0 Ti^{4+} B-site metal configuration [8,24,25,47–54]. Also, it provides an ideal platform for investigations aimed at shedding more light on the perovskite structure tolerance limits under high pressures. In the present study, we explore the limits of the perovskite formability regarding the size of the R constituent and the applied pressure range for R = Tb–Lu in R_2CuTiO_6. We demonstrate a trend of rapidly increasing critical pressure needed for the hexagonal-to-perovskite phase conversion as the size of the R constituent is decreased. A new intermediate phase is observed to occur for Er–Lu between the perovskite and the hexagonal phase regions in the pressure – *versus* – R-size phase diagram. From the steep rise of the border between the hexagonal phase and perovskite with R = Lu we estimate the tolerance parameter value of $t \approx 0.813$ to be a hard limit for the perovskite formation.

2. Experimental

2.1. Sample synthesis

The ambient-pressure (AP) samples were synthesized through conventional solid-state synthesis using starting materials TiO$_2$, CuO, Tb$_4$O$_7$, and R_2O_3 (R = La, Dy-Lu). Hygroscopic rare-earth oxides were pre-heated at 900 °C overnight before weighing to ensure dryness. Stoichiometric (by metal) amounts of the precursors were mixed for 1 h in an agate mortar and then annealed at 1000 °C for 24 h. This step was repeated until no changes in composition were detectable between heating cycles.

The high-pressure (HP) conversions were then carried out for the AP samples for the pressure range of 1–4 GPa using a cubic anvil geometry press (Riken-Seiki; at Aalto University, Finland), following the synthesis procedure of our earlier work for R = Y [46]. Due to calibration limits, the lowest pressure used for the high-pressure treatment was 1 GPa. The AP precursor powder was loaded into a gold capsule, which was assembled into an electrically insulating boronitride sleeve, then into an outer graphite sleeve that functions as an electrical resistance heater, and finally into a pyrophyllite gasket that acts as a solid-state pressure-transfer medium. A portion of ca. 150 mg of the AP precursor was loaded into the gold capsule. The samples were pressed to their target pressure (reached within an hour), then heated to 1000 °C for 40–60 min before quenching and release of pressure. The heating/cooling rate was restricted to maximum 200 °C/min. Synthesis temperature was programmed by calibration (using a NIST standard thermocouple) to electrical load scale, measured in percentile of maximum load capacity of the electric heating system. Active cooling was provided by water flow through the axial anvils at 100–150 ml/min.

The HP treatment at 6 GPa was performed on a multi-anvil press (Rockland Research Corporation, Tecnoprecisa srl 1kton oleodynamic press; at IMEM-CNR in Parma, Italy). The setup consists of an outer set of 6 wedges in cubic geometry, enclosing an inner set of 8 tungsten carbide ISO G2 anvils in octahedral geometry. A similar gasket assembly was used as for the lower-pressure setup: the sample powder was encapsulated in either gold or platinum foil, and then loaded into an assembly of an electrically insulating MgO sleeve inserted into a larger graphite sleeve, all inserted into an octahedral gasket made of magnesium oxide doped with chromium oxide. The assembly included a thermocouple of standard NIST-S for in-situ temperature control, with the thermocouple wire pair connection placed at the surface of the metallic sample capsule. The samples were pressed slowly (overnight) to their target pressure, then heated at 50 °C/min to 900 °C, kept at this temperature for 45 min, and finally cooled at 100 °C/min before releasing the pressure slowly.

2.2. Sample characterization

The phase purity for the AP precursor powders and the phase composition of the HP samples were assessed by powder X-ray diffraction (XRD; PANalytical X'Pert PRO diffractometer; Cu Kα-1 radiation, λ = 1.54 Å). Sample mounting was done by ethanol dispersion of the sample powder on a silicon substrate, let dry before analysis. Rietveld refinements were carried out using FullProf [55,56] software with WinPlotr [57] interface. Choice of starting point unit cell parameters was assisted by SPuDS software [58].

Optical absorption properties were investigated using diffuse reflectance mode on a UV–vis–NIR spectrophotometer over the range 185–1400 nm (Shimadzu UV-2600 spectrometer equipped with ISR-2600 Plus integrating sphere attachment). Sample mounting was identical as for XRD analysis. The obtained absorption spectra were used for calculating an estimate for the optical bandgap (E$_g$) using the Kubelka-Munk transform [59,60] and Tauc plot [61], as previously described in our earlier publication [46].

3. Results and discussion

The XRD patterns for the AP powders confirmed the phase-pure formation of all the intended ambient-pressure precursor phases; the patterns for R = Tb–Lu matched perfectly to the previous entries in the

ICDD and COD databases [25] with non-centrosymmetric space group $P6_3cm$ and the same atomic pattern, which we refer to as "hexagonal" phase (Fig. 1a); the same structure was concluded for our ambient-pressure Y_2CuTiO_6 sample presented in Ref. [46]. The pattern for La_2CuTiO_6, synthesized for comparison, matched with references in the database with space group $Pnma$ [62,63].

All the samples treated under high pressure were found to be converted to a similar orthorhombic perovskite structure as previously seen for the HP-treated Y_2CuTiO_6 in our previous study [46]. However, the pressure needed for the conversion was found to increase with decreasing R^{3+} ionic radius, see Fig. 2. Also, for R = Lu, this conversion was not complete even using 6 GPa (the highest pressure reached in this study). From Fig. 2, it can be seen that the perovskite phase is obtained in phase-pure form e.g. for R = Dy at 1 GPa, for R = Ho at 2 GPa and for R = Yb at 4 GPa. The La_2CuTiO_6 sample pressed at 4 GPa for comparison remained structurally unchanged.

For several of the R constituents, an unidentified intermediate phase was found to form as a side-product at pressures below the critical pressure needed for the complete perovskite-phase formation. This was most evident for the Lu_2CuTiO_6 samples, as seen from the XRD patterns displayed in Fig. 3. The strongest diffraction peak suspected to belong to this intermediate phase is at $2\theta \approx 29.5°$; however, this peak is close to the (110) peak of the hexagonal phase, and thus difficult to quantify. Therefore, we used the "stand-alone" peak appearing at $2\theta \approx 27.65°$ to roughly estimate the relative amounts of the intermediate phase in the different HP samples. The results are visualized in the "pressure versus R size" phase diagram in Fig. 2. For R = Lu, the portion of the intermediate phase first increases with applied pressure up to 3 GPa and then decreases, such that in the 6 GPa sample only traces of this unknown intermediate phase are seen and the orthorhombic perovskite phase dominates. Among the other R constituents, the intermediate phase is barely visible in the R = Ho samples, and clearly seen for the R = Er (1.7 GPa), R = Tm (2–2.5 GPa) and R = Yb (2.5–3.5 GPa) samples. The full-range XRD patterns for all samples are shown in SI.

Unfortunately, we have not yet been able to match the diffraction peaks of the intermediate phase (even for the R = Lu 3 GPa sample) with any structure model. However, similarities in some peak positions, particularly for the strongest peak at $2\theta \approx 33.5°$, lead us to believe that a matching phase could be found within the series of differently stacked hexagonal structures presented in Refs. [17,18]. Another interesting candidate is the garnet structure reported by Sawamoto et al. to form in the border region of the phase conversion seen for $RInO_3$ (R = Eu, Gd, Dy) [39]. We have initiated a follow-up study aiming at obtaining the intermediate phase in single-phase form, which could then allow its structure determination. Since the phase fraction was the largest for the smallest R constituent investigated, we plan to scan the pressure axis with smaller steps for the R = Lu system, in particular in the range from 3 to 4 GPa, and also investigate the possible effect of the applied temperature. Another intersting strategy could be to challenge even smaller
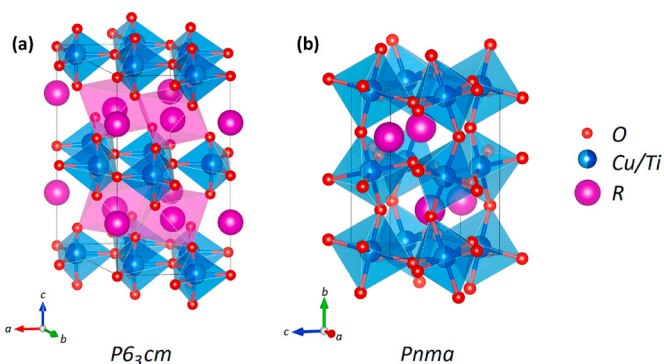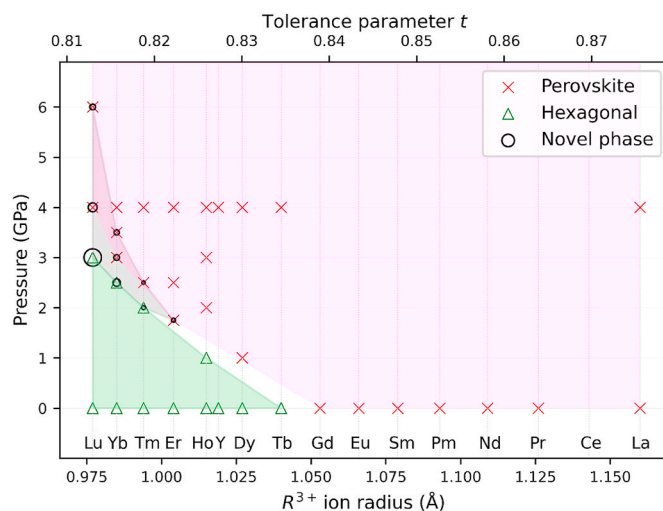

Fig. 2. Pressure versus R^{3+} ion size phase diagram for the R_2CuTiO_6 series (prepared at ca. 1000 °C), showing the appearances of the three different structures: hexagonal, perovskite (with orthorhombic distortion), and the previously unknown intermediate structure; the latter phase is indicated with a black circle, the size of which represents a rough estimation for the relative portion of the phase in the sample. Data for R = Gd–Pr are from Refs. [24,28,53, 62,64–66].
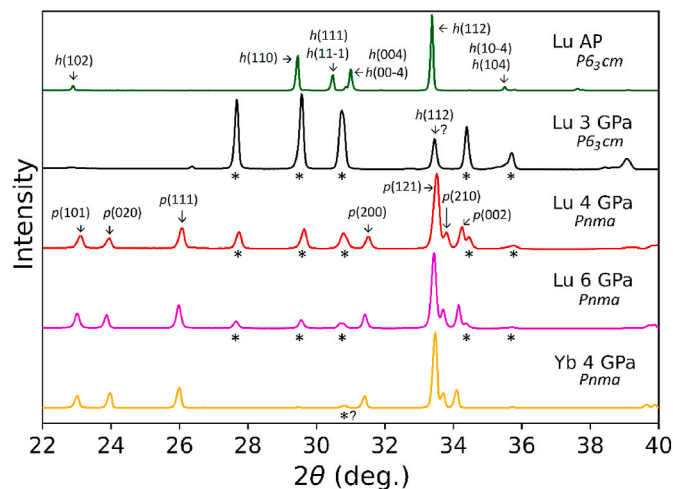

Fig. 3. XRD patterns for the R = Lu samples after HP treatments at different pressures, and for the R = Yb sample HP treated at 4 GPa (for comparison). The peaks marked with a star indicate the presence of the unknown intermediate phase. Full-range XRD patterns for all samples are shown in SI.

R-site constituents towards partially substituted Sc-for-Lu samples.

The targeted orthorhombic perovskite phase (for all the R constituents) was identified to express the same structural features as previously found for the HP sample of Y_2CuTiO_6 [46]. As with the Y_2CuTiO_6 sample, several B-site ordering patterns and thereto connected space groups were evaluated using Rietveld refinement to determine the best-fitting structural model. However, the presence of the unidentified intermediate phase in combination with notable peak broadening for several samples caused complications for the Rietveld refinements. While the unit cell parameters converged well, peak shape fitting proved challenging – and in some cases impossible – due to various degrees of asymmetry in the peak shape. Irregularities in sample surface level, caused by the sample fixation technique, are difficult to account for mathematically in the modelling of the peak shape. In addition, we noted increasing peak broadening with decreasing size of the R^{3+} ion,

Fig. 1. Structure models of (a) the $P6_3cm$ AP phase, and (b) the $Pnma$ HP phase of the R = Tb–Lu samples.

adding to the complexity of the peak shapes especially for the smallest *R*-ion samples. Internal strain caused by the release of pressure after phase formation could explain this trend.

While being able to exclude the structure model with rock-salt type ordering for all samples, we found roughly equal fits for the disordered *Pnma* model (Fig. 1b) and the $P2_1/c$ model with partial layered order at the B site. The $P2_1/c$ models converged to very different levels of B-site order, with no clear trend among the samples, despite the symmetrizing action of the pressure on the crystal structure. For Dy_2CuTiO_6, for which the best Rietveld refinement convergence was obtained, both the HP samples investigated presented a strong preference for layered-site order in the $P2_1/c$ models, but the *Pnma* models converged with equally good fitness parameters and no conclusion on order could thus be made. The results of these refinements are presented in Table 1 and Table 2. The two cases that produced the next-best Rietveld refinement results, namely Tb_2CuTiO_6 and Ho_2CuTiO_6, both converged toward dominant B-site disorder for all samples and ordering models (see data in SI).

Since no conclusive evidence for the presence of B-site ordering could be found, we choose to report the unit cell data for the rest of the sample series obtained by the *Pnma* structure model in Table 3. The detailed list of calculated unit cell parameters and Rietveld refinement parameters can be found in SI. Plotting the unit cell parameters (a, b, c, and volume) as a function of R^{3+} ion radius, we notice an approximately linear trend among the HP-prepared perovskite phases, that differs in angle to the corresponding trend among the R_2CuTiO_6 perovskite phases with the largest *R* constituents (La–Gd) synthesized under ambient pressure. Since all samples prepared under high pressure fit the same structure model, with the same tilting pattern of the octahedral network, it is unsurprising that an increase in A-site R^{3+} ion size results in a corresponding stretching of the unit cell parameters *a*, *b*, and *c* (as visualized in Fig. 4). Meanwhile, for the AP-synthesized *R* = La–Gd phases the structure changes as the R^{3+} ion increases in size. Although the structure and *Pnma* space group remain the same as for the Tb–Lu samples, the tilting gradually decreases for Gd-Nd [28]. Pr_2CuTiO_6 has been reported in both orthorhombic [24] and monoclinic symmetry [67]. In La_2CuTiO_6 the tilting is reduced to 12° in all directions [62]. Changes in tilting are connected with unequal stretching and contraction for the *a*, *b*, and *c* axes, explaining how *a* contracts as *b* and *c* stretch between *R* = Gd and *R* = La [23]. Finally, from the data in Table 3 and Fig. 4, some small deviations from the linearity can be observed, with *R* = Tb and Yb being slightly smaller than the linearity would predict and *R* = Ho slightly larger. These slight deviations can be explained by the somewhat broad XRD peaks (typical for HP samples), leading to inaccuracies in lattice parameter determination. Also, we note that the R^{3+}-ion radii are understood to be imprecise as they are taken from Shannon's listed ionic radii, without accounting for high-pressure effects nor the asymmetric coordination environment in the distorted perovskite structure.

We also like to mention the difference in XRD data quality between the perovskite samples synthesized at different pressures, with peak sharpness appearing to decrease with increasing pressure. This is evident for example for Ho_2CuTiO_6, where e.g. the (212) and (230) peaks (at ca. 48.00° 2θ) are merged for the 4 GPa samples, but increasingly clearly distinguishable for the 3 and 2 GPa samples (Fig. 5).

Table 1

Unit cell parameters for Dy_2CuTiO_6 treated at 4 GPa, refined in space group *Pnma*: a = 5.74123(3) Å, b = 7.47561(4) Å, c = 5.32178(3) Å; R_p = 2.55, R_{wp} = 4.18, and R_{Bragg} = 6.68.

	x	y	z	Occ
Dy	0.57526(17)	0.25	0.4830(3)	1.
Cu	0	0	0	0.5
Ti	0	0	0	0.5
O1	−0.0373(16)	0.25	0.6078(16)	1.
O2	0.1882(13)	−0.0588(9)	0.8094(13)	1.

Table 2

Unit cell parameters for Dy_2CuTiO_6 treated at 4 GPa, refined in space group $P2_1/c$: a = 7.47560(4) Å, b = 5.32178(3) Å, c = 5.74123(3) Å, β = 90.005(3)°; R_p = 2.58, R_{wp} = 4.25, and R_{Bragg} = 7.06.

	x	y	z	Occ
Dy	0.25100	−0.0169	0.07527	1.
Cu	0.	0.	0.5	0.17(10)
Ti	0.	0.	0.5	0.83(10)
Ti	0.5	0.	0.5	0.17(10)
Cu	0.5	0.	0.5	0.83(10)
O1	0.22293	0.10722	0.46177	1.
O2	−0.0653	0.30642	0.71102	1.
O3	0.44061	0.68453	0.33518	1.

Table 3

Summary of the unit cell parameters for the sample series, as refined in space group *Pnma*. A complete list of sample-specific unit cell and Rietveld refinement parameters can be found in SI.

| R^{3+}-ion	a (Å)	b (Å)	c (Å)	V (Å³)	Phase purity	Reference
Tb	5.7474	7.4912	5.3394	229.9	Pure perovskite	This work
Dy	5.7412	7.4756	5.3218	228.4	Pure perovskite	This work
Y	7.4572	5.2965	5.7305	226.3	Pure perovskite	[46]
Ho	5.3013	7.4642	5.7351	227.0	Pure perovskite	This work
Er	5.7225	7.4446	5.2799	225.0	Pure perovskite	This work
Tm	5.7049	7.4331	5.2670	223.4	Perovskite dominant	This work
Yb	5.6915	7.4173	5.2540	221.8	Perovskite dominant	This work
Lu	5.6769	7.4262	5.2350	220.7	Mixed	This work
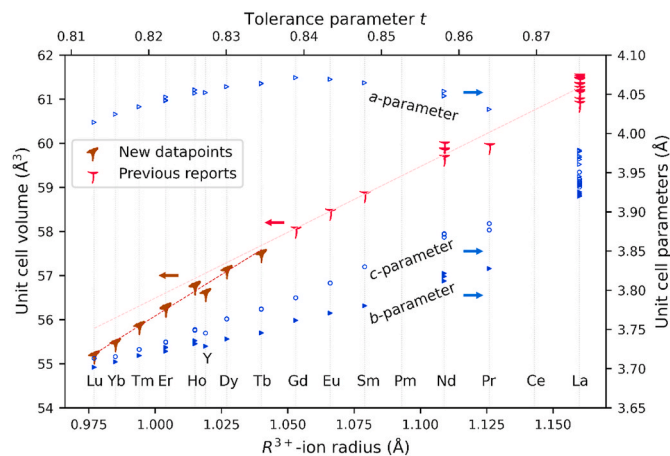
Fig. 4. Normalized unit cell parameters of perovskite R_2CuTiO_6 samples plotted as a function of R^{3+}-ion radius (as defined by Shannon for CN = 8). For comparison with previously reported structures, the values in the plot are normalized to single perovskite (Z = 1) values. Corresponding tolerance parameter values are shown at the top of the plot. Data for *R* = Gd–Pr are from Refs. [24,28,53,62,64–66].

The same trend is visible when comparing the Er_2CuTiO_6 samples made at 2.5 and 4 GPa. The sample made at 1.7 GPa (the lowest pressure investigated for *R* = Er) presented an impurity phase associated with the border zone, and also broader peaks for the perovskite phase. We interpret that the sample is near the perovskite-forming minimum pressure, and this might affect the structure to make the peaks broader. In Tm_2CuTiO_6 the trend is less obvious; a small difference in peak separation is discernible between the (123) and (232) peaks (at ca 60.50° 2θ), but the (212)/(230) peak pair is fused. The Yb_2CuTiO_6 sample series shows a presence of the intermediate phase across a wider pressure range, including the sample made at 3 GPa which nevertheless expresses
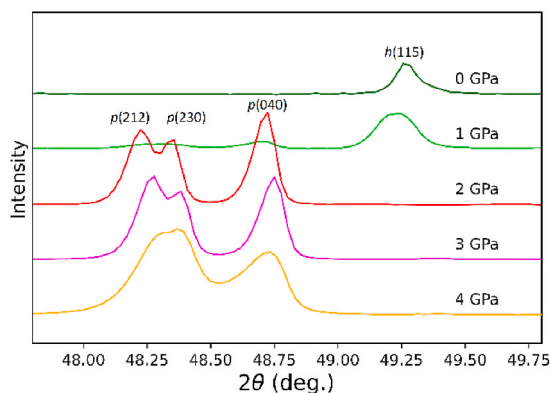
Fig. 5. The 48-50° 2θ region for the series of Ho_2CuTiO_6 samples prepared at (from the bottom) 4 GPa, 3 GPa, 2 GPa, 1 GPa, and ambient pressure. The phase transition between 1 GPa and 2 GPa is clearly noticeable. The peak sharpness in the perovskite samples is seen to decrease with increased synthesis pressure, with clear peak separation of (212) and (230) in the 2 GPa sample progressing to no peak separation in the 4 GPa sample.

the sharpest separation between the (212)/(230) peaks (fused) and (040), and also between peaks (123) and (232).

We suggest that the blurring of the peaks for samples synthesized well above the critical pressure could come from unit cell strains appearing upon release of pressure. Octahedral tilting is known to be affected by high physical pressure. For example, with Ho_2CuTiO_6 the sample prepared at 4 GPa might crystallize with a different octahedral tilting pattern than the one made at 2 GPa: upon release of pressure, the octahedral network might not be able to move freely to relax into the tilting pattern preferred at the lowest pressure at which distorted perovskite phase is able to form. This could be a source of internal strain, which can cause peak broadening as a result of local deformation and

altering of the interplanar distances in the strained unit cells.

Finally, we present the UV–vis absorption spectra for the samples in Fig. 6 to illustrate the phase changes from the sample colour point of view. With increasing synthesis pressure, absorption spectra of the hexagonal samples start expressing changes: most notable is the overall broadening of the reflectance peak in the visible spectrum and lowering of its intensity maximum at ca. 550 nm. This trend is visible for all sample series where hexagonal phase was obtained at multiple pressures (all spectra are shown in SI). It also corresponds with visible changes in sample colour, from subtly different shades of forest green to slightly darker green nuances. As the XRD patterns clearly show that the phase remains unchanged between hexagonal samples prepared at different pressures, we interpret these changes in reflectance to be an effect of bond length compression caused by the high-pressure treatment.

The spectra undergo a clear transformation when the sample phase changes to orthorhombic perovskite. The peak maximum at 550 nm is extinguished and a new, much lower maximum appears towards the red end of the visible light spectrum range, marking the beginning of a reflectance plateau extending into the infrared spectrum. Comparing perovskite samples of the same composition, the differences between spectra are mostly limited to overall intensity variations between different scans. The overall intensity differences can be explained by the sample fixation method producing slightly different sample coverage of the sample holder.

Based on the absorption spectra, the novel intermediate phase in the $R = Lu$ 3 GPa sample is very evidently different from both the AP sample and the perovskite sample features (Fig. 6 c). In the visible spectrum range, this sample expresses a nearly flat region, slightly higher toward the blue end of the spectrum. The low-energy side absorption limit is also at much lower wavelength at ca. 850 nm (ca. 1.5 eV) than for either the hexagonal or perovskite phase (ca. 1000 nm, 1.3 eV).

Optical bandgaps calculated from the Kubelka-Munk-Tauc transformed UV–vis data showed roughly similar values for all samples, fluctuating between 3.3 and 3.5 eV with no detectable trends regarding
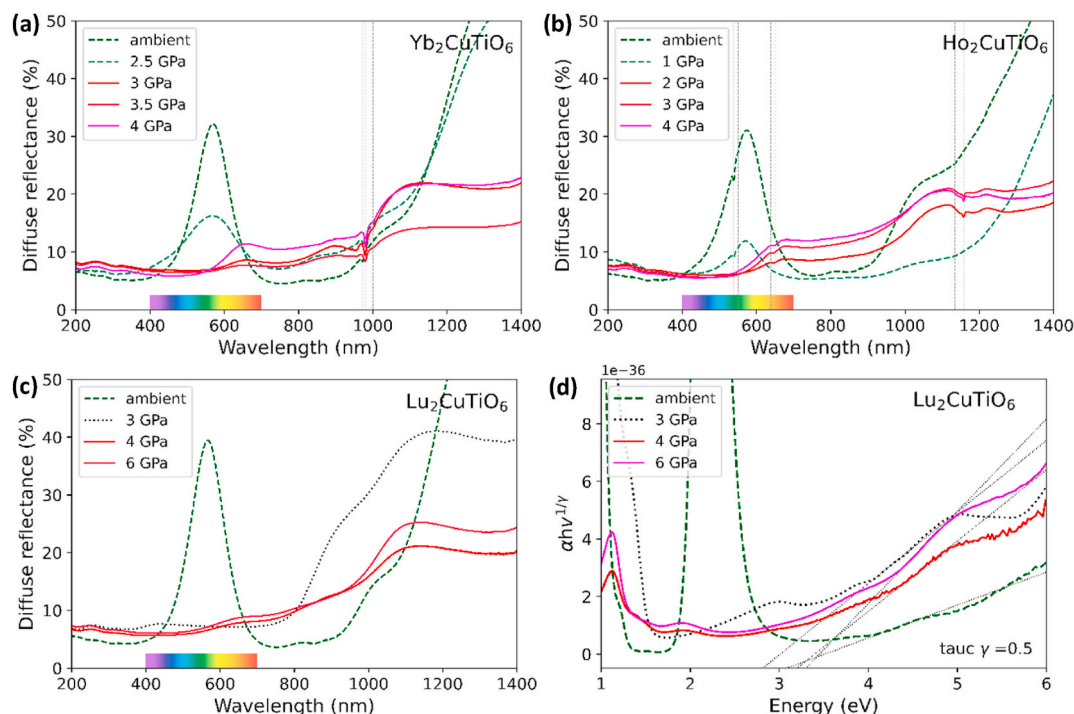

Fig. 6. Absorption spectra of (a) $R = Yb$, (b) Ho, and (c) Lu sample series; (d) the corresponding Kubelka-Munk-Tauc transformed data for Lu_2CuTiO_6. The difference between the different-phase samples is clear throughout the spectra; the phase change is even visible to the naked eye in the reflectance peak centred around 550 nm of the hexagonal phase samples, which present different green colours (plotted with dashed green-blue lines for both plots). This peak is extinguished for the perovskite phase samples that in turn appear dark brown in colour (plotted with continuous red-orange lines), and in the new intermediate-phase sample (black, dotted) which appears grey-black. The vertical lines mark the detected positions of the lanthanide absorption bands.

the phase nor the *R* constituent. These values are comparable with the bandgap we have reported for Y_2CuTiO_6, for which bandgap calculations by DFT calculations (3.1–3.3 eV) agreed with the result given by the Kubelka-Munk-Tauc method (ca. 3.6 eV) [46]. Only the *R* = Lu 3 GPa sample, concluded also by XRD to present the largest amount of the unknown intermediate phase, expressed a lower bandgap value of ca. 3.0 eV. However, we point out that the precision of these calculations is limited by the imprecision in interpretation of the energy interval that is best representative of the linear range that marks the onset of the absorption edge. From the plotted data, the exact position of the correct linear range is challenging to determine, especially so for the Lu_2CuTiO_6 3 GPa sample. Thus, we must conclude that these bandgap values should be interpreted as rough estimates only.

4. Conclusions

We have investigated the applied pressure/phase formation diagram for the R_2CuTiO_6 system in the applied pressure range up to 6 GPa for the rare earth element constituents from Tb to Lu. These *R* constituents are the ones for which conventional ambient-pressure synthesis yields the R_2CuTiO_6 mixed-metal oxide with the hexagonal non-perovskite structure, similarly to several other *R*-based hexagonal systems such as the $RMnO_3$ manganites.

We employed both X-ray diffraction and UV–vis spectroscopy to systematically follow the pressure-driven phase transformations within the R_2CuTiO_6 system. With decreasing size of the R^{3+} ion, increasingly high pressures are required to convert the R_2CuTiO_6 compounds to the perovskite structure. For the smallest Lu, this critical pressure was found to be ca. 6 GPa. For all the *R* constituents investigated from Tb to Lu, the resultant R_2CuTiO_6 perovskite structure showed an orthorhombic distortion described by the space group *Pnma*.

As an exciting observation, a novel intermediate phase was found to form for most of the *R* constituents when pressures close to the critical pressure were applied. The relative amount and the pressure stability range of this previously unreported phase were the largest for the smallest *R* constituent, Lu. Nevertheless, despite considerable efforts the crystal structure of the intermediate phase remained undefined, although implications could be noticed for example to an intermediate phase previously seen for the *R*InO_3 system. Further investigations with varied high-pressure treatment conditions are ongoing to learn more about this phase.

Another general observation was that the applied pressure beyond the critical perovskite-formation pressure tended to decrease the sharpness of XRD peaks. Tentatively, we explain this as the consequence of unit cell strains appearing upon the release of applied pressure.

Finally, it should be emphasized that the present results and conclusions for the R_2CuTiO_6 compounds should be rather straightforwardly transferable to many other interesting perovskite systems based on different rare earth elements (or alternatively e.g. different alkaline earth elements) as the A-site constituents, to provide further understanding on the pressure-driven structural transformations in these systems.

CRediT authorship contribution statement

Linda Sederholm: Writing – original draft, Visualization, Methodology, Investigation, Conceptualization. **Edmondo Gilioli:** Resources, Methodology. **Davide Delmonte:** Resources, Methodology. **Ayako Yamamoto:** Validation, Methodology. **Maarit Karppinen:** Writing – review & editing, Supervision, Resources, Funding acquisition, Conceptualization.

Declaration of competing interest

The authors declare that they have no known competing financial interests or personal relationships that could have appeared to influence the work reported in this paper.

Data availability

Data will be made available on request.

Appendix A. Supplementary data

Supplementary data to this article can be found online at https://doi.org/10.1016/j.solidstatesciences.2024.107514.

References

[1] J.P. Attfield, P. Lightfoot, R.E. Morris, Perovskites, Dalton Trans. 44 (2015) 10541–10542, https://doi.org/10.1039/C5DT90083B.

[2] A. Maignan, C. Martin, D. Pelloquin, N. Nguyen, B. Raveau, Structural and magnetic studies of ordered oxygen-deficient perovskites LnBaCo$_2$O$_{5+\delta}$, closely related to the "112" structure, J. Solid State Chem. 142 (1999) 247–260, https://doi.org/10.1006/jssc.1998.7934.

[3] N. Imamura, M. Karppinen, T. Motohashi, D. Fu, M. Itoh, H. Yamauchi, Positive and negative magnetodielectric effects in *A*-site ordered (BiMn$_3$)Mn$_4$O$_{12}$ perovskite, J. Am. Chem. Soc. 130 (2008) 14948–14949, https://doi.org/10.1021/ja806487d.

[4] E. Solana-Madruga, C. Ritter, C. Aguilar-Maldonado, O. Mentré, J.P. Attfield, Á. M. Arévalo-López, Mn$_3$MnNb$_2$O$_9$: high-pressure triple perovskite with 1:2 B-site order and modulated spins, Chem. Commun. 57 (2021) 8441–8444, https://doi.org/10.1039/D1CC02782D.

[5] S. Vasala, M. Karppinen, A$_2$B'B"O$_6$ perovskites: a review, Prog. Solid State Chem. 43 (2015) 1–36, https://doi.org/10.1016/j.progsolidstchem.2014.08.001.

[6] T. Stoyanova-Lyubenova, A.J. Dos santos-García, E. Urones-Garrote, M.J. Torralvo, M.Á. Alario-Franco, High-pressure synthesis, structural and complex magnetic properties of the ordered double perovskite Pb$_2$NiReO$_6$, Dalton Trans. 43 (2014) 1117–1124, https://doi.org/10.1039/C3DT52073K.

[7] R. Morrow, J. Yan, M.A. McGuire, J.W. Freeland, D. Haskel, P.M. Woodward, Effects of chemical pressure on the magnetic ground states of the osmate double perovskites SrCaCoOsO$_6$ and Ca$_2$CoOsO$_6$, Phys. Rev. B 92 (2015) 094435, https://doi.org/10.1103/PhysRevB.92.094435.

[8] D. Iwanaga, Y. Inaguma, M. Itoh, Crystal structure and magnetic properties of B-site ordered perovskite-type oxides A$_2$CuB'O$_6$ (A=Ba, Sr; B'=W, Te), J. Solid State Chem. 147 (1999) 291–295, https://doi.org/10.1006/jssc.1999.8273.

[9] G. King, P.M. Woodward, Cation ordering in perovskites, J. Mater. Chem. 20 (2010) 5785–5796, https://doi.org/10.1039/B926757C.

[10] Y.H. Huang, J. Lindén, H. Yamauchi, M. Karppinen, Simple and efficient route to prepare homogeneous samples of Sr$_2$FeMoO$_6$ with a high degree of Fe/Mo order, Chem. Mater. 16 (2004) 4337–4342, https://doi.org/10.1021/cm0493288.

[11] S. Vasala, M. Lehtimäki, Y.H. Huang, H. Yamauchi, J.B. Goodenough, M. Karppinen, Degree of order and redox balance in B-site ordered double-perovskite oxides, Sr$_2$*M*MoO$_{6-\delta}$ (*M*=Mg, Mn, Fe, Co, Ni, Zn), J. Solid State Chem. 183 (2010) 1007–1012, https://doi.org/10.1016/j.jssc.2010.03.004.

[12] G.M. McNally, A.M. Arévalo-López, F. Guillou, P. Manuel, J.P. Attfield, Evolution of cation and spin orders in the double–double-double perovskite series Ca$_x$Mn$_{2-x}$FeReO$_6$, Phys. Rev. Mater. 4 (2020) 064408, https://doi.org/10.1103/PhysRevMaterials.4.064408.

[13] V.M. Goldschmidt, Die Gesetze der Krystallochemie, Naturwissenschaften 14 (1926) 477–485, https://doi.org/10.1007/BF01507527.

[14] R.D. Shannon, Revised effective ionic radii and systematic studies of interatomic distances in halides and chalcogenides, Acta Crystallogr. A 32 (1976) 751–767, https://doi.org/10.1107/S0567739476001551.

[15] A.M. Glazer, The classification of tilted octahedra in perovskites, Acta Crystallogr. B 28 (1972) 3384–3392, https://doi.org/10.1107/S0567740872007976.

[16] M.R. Filip, F. Giustino, The geometric blueprint of perovskites, Proc. Natl. Acad. Sci. USA 115 (2018) 5397–5402, https://doi.org/10.1073/pnas.1719179115.

[17] Y. Syono, S. Akimoto, K. Kohn, Structure relations of hexagonal perovskite-like compounds ABX$_3$ at high pressure, J. Phys. Soc. Japan 26 (1969) 993–999, https://doi.org/10.1143/JPSJ.26.993.

[18] J.F. Vente, P.D. Battle, Structural chemistry and electronic properties of the hexagonal perovskites BaIr$_{1-x}$Co$_x$O$_{3-\delta}$ (x = 0.5, 0.7, 0.8), J. Solid State Chem. 152 (2000) 361–373, https://doi.org/10.1006/jssc.2000.8664.

[19] R.C. DeVries, R. Roy, Phase equilibria in the system BaTiO$_3$–CaTiO$_3$, J. Am. Ceram. Soc. 38 (1955) 142–146, https://doi.org/10.1111/j.1151-2916.1955.tb14918.x.

[20] H.L. Yakel Jnr, W.C. Koehler, E.F. Bertaut, E.F. Forrat, On the crystal structure of the manganese(III) trioxides of the heavy lanthanides and yttrium, Acta Crystallogr. 16 (1963) 957–962, https://doi.org/10.1107/S0365110X63002589.

[21] B. Paul, S. Chatterjee, S. Gop, A. Roy, V. Grover, R. Shukla, A.K. Tyagi, Evolution of lattice dynamics in ferroelectric hexagonal $REInO_3$ (RE = Ho, Dy, Tb, Gd, Eu, Sm) perovskites, Mater. Res. Express 3 (2016) 075703, https://doi.org/10.1088/2053-1591/3/7/075703.

[22] K. Naveen, N. Kumar, T.K. Mandal, P.D. Babu, V. Siruguri, P.K. Maji, A.K. Paul, Multiferroic behaviour in B-site Cr-doped hexagonal $YInO_3$ perovskites: synthesis, structure and properties, J. Mol. Struct. 1185 (2019) 432–439, https://doi.org/10.1016/j.molstruc.2019.02.099.

[23] K. Uusi-Esko, J. Malm, N. Imamura, H. Yamauchi, M. Karppinen, Characterization of $RMnO_3$ (R = Sc, Y, Dy-Lu): high-pressure synthesized metastable perovskites and their hexagonal precursor phases, Mater. Chem. Phys. 112 (2008) 1029–1034, https://doi.org/10.1016/j.matchemphys.2008.07.009.

[24] K. Singh, N. Kumar, B. Singh, S.D. Kaushik, N.K. Gaur, S. Bhattacharya, S. Rayaprol, C. Simon, Magnetic and dielectric properties of R_2CuTiO_6 compounds (R=Y, La, Pr and Nd), J. Supercond. Nov. Magnetism 24 (2011) 1829–1838, https://doi.org/10.1007/s10948-011-1131-7.

[25] N. Floros, J.T. Rijssenbeek, A.B. Martinson, K.R. Poeppelmeier, Structural study of A_2CuTiO_6 (A=Y, Tb–Lu) compounds, Solid State Sci. 4 (2002) 1495–1498, https://doi.org/10.1016/S1293-2558(02)00045-6.

[26] S.B. Reddy, K. Mohan Kant, K.P. Rao, M. Opel, R. Gross, M.S.R. Rao, Ferroelectric and magnetic properties of Ho_2CuTiO_6 double perovskite, J. Magn. Magn. Mater. 303 (2006) e332–e334, https://doi.org/10.1016/j.jmmm.2006.01.101.

[27] D. Choudhury, A. Hazarika, A. Venimadhav, C. Kakarla, K.T. Delaney, P.S. Devi, P. Mondal, R. Nirmala, J. Gopalakrishnan, N.A. Spaldin, U.V. Waghmare, D. D. Sarma, Electric and magnetic polarizabilities of hexagonal Ln_2CuTiO_6 (Ln=Y, Dy, Ho, Er, and Yb), Phys. Rev. B 82 (2010) 134203, https://doi.org/10.1103/PhysRevB.82.134203.

[28] Z. Yang, W. Wong-Ng, J.-A. Kaduk, M. Jang, G. Liu, Phase equilibria and crystal chemistry of the R–Cu–Ti–O systems (R=lanthanides and Y), J. Solid State Chem. 182 (2009) 1142–1148, https://doi.org/10.1016/j.jssc.2008.11.010.

[29] J.A. Kafalas, J.M. Longo, Effect of pressure on the structure and magnetic properties of $RbNiF_3$, Mater. Res. Bull. 3 (1968) 501–506, https://doi.org/10.1016/0025-5408(68)90074-3.

[30] J.M. Longo, J.A. Kafalas, Pressure-induced structural changes in the system $Ba_{1-x}Sr_xRuO_3$, Mater. Res. Bull. 3 (1968) 687–692, https://doi.org/10.1016/0025-5408(68)90118-9.

[31] T. Tiittanen, M. Karppinen, Structure evolution upon chemical and physical pressure in $(Sr_{1-x}Ba_x)_2FeSbO_6$, J. Solid State Chem. 246 (2017) 245–251, https://doi.org/10.1016/j.jssc.2016.11.033.

[32] K. Nishimura, I. Yamada, K. Oka, Y. Shimakawa, M. Azuma, High-pressure synthesis of $BaVO_3$: a new cubic perovskite, J. Phys. Chem. Solid. 75 (2014) 710–712, https://doi.org/10.1016/j.jpcs.2014.02.001.

[33] T. Aoba, T. Tiittanen, H. Suematsu, M. Karppinen, Pressure-induced phase transitions of hexagonal perovskite-like oxides, J. Solid State Chem. 233 (2016) 492–496, https://doi.org/10.1016/j.jssc.2015.11.028.

[34] C. Lin, J. Liu, Y. Li, X. Li, R. Li, Pressure-induced structural and vibrational evolution in ferroelectric $RInO_3$ (R = Eu, Gd, Dy), Solid State Commun. 173 (2013) 51–55, https://doi.org/10.1016/j.ssc.2013.09.006.

[35] A. Dwivedi, H.K. Poswal, R. Shukla, S. Velaga, B.D. Sahoo, V. Grover, M.N. Deo, High pressure structural investigations on hexagonal $YInO_3$, High Pres. Res. 39 (2019) 17–35, https://doi.org/10.1080/08957959.2018.1557162.

[36] Z. Deng, C. Kang, M. Croft, W. Li, X. Shen, J. Zhao, R. Yu, C. Jin, G. Kotliar, S. Liu, T.A. Tyson, R. Tappero, M. Greenblatt, A pressure-induced inverse order–disorder transition in double perovskites, Angew. Chem. 132 (2020) 8317–8323, https://doi.org/10.1002/ange.202001922.

[37] P. Gao, Z. Chen, T.A. Tyson, T. Wu, K.H. Ahn, Z. Liu, R. Tappero, S.B. Kim, S.-W. Cheong, High-pressure structural stability of multiferroic hexagonal $RMnO_3$ (R = Y, Ho, Lu), Phys. Rev. B 83 (2011) 224113, https://doi.org/10.1103/PhysRevB.83.224113.

[38] A. Waintal, J. Chenavas, Transformation sous haute pression de la forme hexagonale de $MnT'O_3$ (T' = Ho, Er, Tm, Yb, Lu) en une forme perovskite, Mater. Res. Bull. 2 (1967) 819–822, https://doi.org/10.1016/0025-5408(67)90009-8.

[39] H. Sawamoto, High-pressure synthesis of perovskite type $RInO_3$ (R=Eu, Gd, and Dy), Jpn. J. Appl. Phys. 12 (1973) 1432–1438, https://doi.org/10.1143/JJAP.12.1432.

[40] M. Marezio, J.P. Remeika, P.D. Dernier, High pressure synthesis of $YGaO_3$, $GdGaO_3$ and $YbGaO_3$, Mater. Res. Bull. 1 (1966) 247–255, https://doi.org/10.1016/0025-5408(66)90011-0.

[41] H. Okamoto, N. Imamura, B.C. Hauback, M. Karppinen, H. Yamauchi, H. Fjellvåg, Neutron powder diffraction study of crystal and magnetic structures of orthorhombic $LuMnO_3$, Solid State Commun. 146 (2008) 152–156, https://doi.org/10.1016/j.ssc.2008.01.036.

[42] F. Sugawara, Y. Syono, S. Akimoto, High pressure synthesis of a new perovskite $PbSnO_3$, Mater. Res. Bull. 3 (1968) 529–532, https://doi.org/10.1016/0025-5408(68)90078-0.

[43] F. Sugawara, S. Iiida, Y. Syono, S. Akimoto, Magnetic properties and crystal distortions of $BiMnO_3$ and $BiCrO_3$, J. Phys. Soc. Japan 25 (1968) 1553–1558, https://doi.org/10.1143/JPSJ.25.1553.

[44] B.L. Chamberland, Preparation and properties of $SrCrO_3$, Solid State Commun. 5 (1967) 663–666, https://doi.org/10.1016/0038-1098(67)90088-9.

[45] J. Liebertz, C.J.M. Rooymans, Die Ilmenit/Perowskit-Phasenumwandlung von $CdTiO_3$ unter hohem Druck, Z. Phys. Chem. 44 (1965) 242–249, https://doi.org/10.1524/zpch.1965.44.3_4.242.

[46] L. Sederholm, T. Tiittanen, M. Karppinen, High-pressure stabilisation of R = Y member of R_2CuTiO_6 double perovskite series, J. Solid State Chem. 317 (2023) 123646, https://doi.org/10.1016/j.jssc.2022.123646.

[47] O. Mustonen, S. Vasala, E. Sadrollahi, K.P. Schmidt, C. Baines, H.C. Walker, I. Terasaki, F.J. Litterst, E. Baggio-Saitovitch, M. Karppinen, Spin-liquid-like state in a spin-½ square-lattice antiferromagnet perovskite induced by d^{10}–d^0 cation mixing, Nat. Commun. 9 (2018) 1085, https://doi.org/10.1038/s41467-018-03435-1.

[48] O. Mustonen, S. Vasala, K.P. Schmidt, E. Sadrollahi, H.C. Walker, I. Terasaki, F. J. Litterst, E. Baggio-Saitovitch, M. Karppinen, Tuning the S=½ square-lattice antiferromagnet $Sr_2Cu(Te_{1-x}W_x)O_6$ from Néel order to quantum disorder to columnar order, Phys. Rev. B 98 (2018) 064411, https://doi.org/10.1103/PhysRevB.98.064411.

[49] E. Fogh, O. Mustonen, P. Babkevich, V.M. Katukuri, H.C. Walker, L. Mangin-Thro, M. Karppinen, S. Ward, B. Normand, H.M. Rønnow, Randomness and frustration in a S = ½ square-lattice Heisenberg antiferromagnet, Phys. Rev. B 105 (2022) 184410, https://doi.org/10.1103/PhysRevB.105.184410.

[50] V.M. Katukuri, P. Babkevich, O. Mustonen, H.C. Walker, B. Fåk, S. Vasala, M. Karppinen, H.M. Rønnow, O. V Yazyev, Exchange interactions mediated by nonmagnetic cations in double perovskites, Phys. Rev. Lett. 124 (2020) 077202, https://doi.org/10.1103/PhysRevLett.124.077202.

[51] O. Mustonen, S. Vasala, H. Mutch, C.I. Thomas, G.B.G. Stenning, E. Baggio-Saitovitch, E.J. Cussen, M. Karppinen, Magnetic interactions in the S = ½ square-lattice antiferromagnets Ba_2CuTeO_6 and Ba_2CuWO_6: parent phases of a possible spin liquid, Chem 55 (2019) 1132–1135, https://doi.org/10.1039/c8cc09479a.

[52] H.C. Walker, O. Mustonen, S. Vasala, D.J. Voneshen, M.D. Le, D.T. Adroja, M. Karppinen, Spin wave excitations in the tetragonal double perovskite Sr_2CuWO_6, Phys. Rev. B 94 (2016) 064411, https://doi.org/10.1103/PhysRevB.94.064411.

[53] W.Z. Yang, M.M. Mao, X.Q. Liu, X.M. Chen, Structure and dielectric relaxation of double-perovskite La_2CuTiO_6 ceramics, J. Appl. Phys. 107 (2010) 124102, https://doi.org/10.1063/1.3446846.

[54] D. Choudhury, D.D. Sarma, Robust dielectric properties of B-site size-disordered hexagonal Ln_2CuTiO_6 (Ln=Dy, Ho, Er, and Yb), J. Vac. Sci. Technol. B 32 (2014) 03D118, https://doi.org/10.1116/1.4868112.

[55] J. Rodriguez-Carvajal, FullProf(software), version sep-2020, Complete program and documentation can be obtained from, https://www.ill.eu/sites/fullprof/index.html.

[56] J. Rodríguez-Carvajal, Recent advances in magnetic structure determination by neutron powder diffraction, Phys. B: Condens. Matter 192 (1993) 55–69, https://doi.org/10.1016/0921-4526(93)90108-I.

[57] T. Roisnel, J. Rodríquez-Carvajal, WinPLOTR: a windows tool for powder diffraction pattern analysis, Mater. Sci. Forum (2001) 378–381. https://dx.doi.org/10.4028/www.scientific.net/MSF.378-381.118, 118–123.

[58] M.W. Lufaso, P.M. Woodward, Prediction of the crystal structures of perovskites using the software program SPuDS, Acta Crystallogr. B 57 (2001) 725–738, https://doi.org/10.1107/S0108768101015282.

[59] P. Kubelka, F. Munk, Ein Beitrag zur Optik der Farbanstriche (An article on optics of paint layers), Z. Tech. Phys. 12 (1931) 593–601.

[60] P. Makula, M. Pacia, W. Macyk, How to correctly determine the band gap energy of modified semiconductor photocatalysts based on UV-Vis spectra, J. Phys. Chem. Lett. 9 (2018) 6814–6817, https://doi.org/10.1021/acs.jpclett.8b02892.

[61] J. Tauc, Optical properties and electronic structure of amorphous Ge and Si, Mater. Res. Bull. 3 (1968) 37–46, https://doi.org/10.1016/0025-5408(68)90023-8.

[62] M.R. Palacín, J. Bassas, J. Rodríguez-Carvajal, P. Gómez-Romero, Syntheses of the perovskite La_2CuTiO_6 by the ceramic, oxide precursors and sol–gel methods, and study of the structure and Cu–Ti distribution by X-ray and neutron diffraction, J. Mater. Chem. 3 (1993) 1171–1177, https://doi.org/10.1039/JM9930301171.

[63] M.R. Palacín, J. Bassas, J. Rodríguez-Carvajal, A. Fuertes, N. Casañ-Pastor, P. Gómez-Romero, Studies of the formation and reduction of a mixed three-dimensional perovskite of copper and titanium, Mater. Res. Bull. 29 (1994) 973–980, https://doi.org/10.1016/0025-5408(94)90058-2.

[64] N. Ramadass, J. Gopalakrishnan, M.V.C. Sastri, Preparation and characterization of La_2TiMO_6 (M = Co, Ni, Cu and Zn) perovskites, J. Inorg. Nucl. Chem. 40 (1978) 1453–1454, https://doi.org/10.1016/0022-1902(78)80072-4.

[65] P. Gomez-Romero, M. Palacin, N. Casan, A. Fuertes, B. Martinez, Towards the synthesis of layered perovskites. Synthesis, structure and magnetic properties of La_2CuTiO_6, Solid State Ionics 63–65 (1993) 603–608, https://doi.org/10.1016/0167-2738(93)90166-Z.

[66] M.T. Anderson, K. Greenwood, G. Taylor, K. Poeppelmeier, B-cation arrangements in double perovskites, Prog. Solid State Chem. 22 (1993) 197–233, https://doi.org/10.1016/0079-6786(93)90004-B.

[67] D.K. Mahato, T.P. Sinha, Dielectric, impedance and conduction behavior of double perovskite Pr_2CuTiO_6 ceramics, J. Electron. Mater. 46 (2017) 107–115, https://doi.org/10.1007/s11664-016-4842-5.